

Research

Study of a wall-climbing robot based on chain feet with negative pressure adhesion

Zhen Qian¹ · Hanbiao Xia²

Received: 15 May 2023 / Accepted: 6 March 2024

Published online: 14 March 2024

© The Author(s) 2024 [OPEN](#)

Abstract

In this paper, a wall-climbing robot based on chain feet with negative pressure adhesion is designed. The robot uses chain feet with negative pressure adhesion as the motion units and has the characteristics of adhesion and barrier crossing. Analyzing the power consumption is an important aspect of robot design. The influences of robot design parameters on mechanical characteristics are analyzed with the kinetic method. The robot power model is constructed by combining the energy model of the drive motor and the power model of the transmission system. The relationship between the key parameters and robot power consumption is established by discussing the effects of the robot load, motor angular velocity, and other related design parameters on the robot power consumption. Simulations and experiments show that the established robot power model can be used as a theoretical basis for the optimal design of robots and provides a reference for establishing an optimal model for the motion control of robots.

Article Highlights

- The wall-climbing robot has a special structure that achieves adhesion. For example, chain feet are structures that can attain negative pressure adhesion.
- The individual design parameters of this robot's motion module have different effects on its mechanical properties.
- The power model constructed by the robot can reveal the relationship between the structural parameters and power consumption.

1 Introduction

The development of hardware structures and artificial intelligence has led to significant advancements in the design of wall-climbing robots [1]. Therefore, such robots have begun to be widely used in many areas of life. For example, air channels in hospitals contain germs and need to be cleaned regularly. Traditional artificial cleaning methods are expensive and inefficient and may cause an increased risk of infection. Using wall-climbing robots instead of manual labor can prevent infections. Thus, properly designing wall-climbing robots is very important.

Wall-climbing robots have received increasing attention from scholars for their efficient operation efficiency and adaptability to walls [2]. Currently, the main robot adhesion methods are negative pressure adhesion [3], magnetic adhesion [4], bionic adhesion [5], thrust adhesion [6], adhesive adhesion [7] and electrostatic adhesion [8]. Among them, the magnetic

✉ Zhen Qian, zhenqian@wmu.edu.cn | ¹The First Affiliated Hospital of Wenzhou Medical University, Wenzhou, China. ²College of Mechanical Engineering, Zhejiang University of Technology, Hangzhou, China.



adhesion method is divided into electromagnetic adhesion and permanent magnet adhesion with a large and adjustable adhesion force. However, it can only be applied to the surface of a magnetic conductor. The bionic adhesion method is inspired by animal movement and can adsorb on rough walls. However, the adhesion force is limited, and the production cost is high. The advantage of vacuum negative pressure adhesion is that it is not limited by the material of the working surface and is applicable to several types of robots. The wall-climbing robot requires a good movement method to ensure a sufficient speed and strong adaptability in areas such as the air channels in a hospital. At present, more studied movement methods include the frame type [9], leg-foot type [10], and crawler type [11]. Among them, the frame type has a smooth structure and a strong adhesion force. However, it operates slowly and is difficult to steer. The leg-foot type has a strong obstacle-crossing ability, but it also moves slowly and is difficult to control. By combining multiple movement methods, the performance of wall-climbing robots can be improved.

Energy is necessary for robots to accomplish their tasks [12]. The special structure and motion of wall-climbing robots increase their energy consumption. Compared to ordinary mobile robots, wall-climbing robots consume more energy. Moreover, the distribution of hospital air ducts is intricate and complex. The higher power consumption of the robot can significantly affect the coverage and repetition rate of the operation. Thus, possible energy complexities will greatly limit the robot's ability to complete tasks [13]. Researchers have proposed many optimization methods and algorithms, including models of robot energy consumption [14], trajectory optimization [15], and task planning [16]. These studies can help to analyze the energy consumption of mobile robots. However, wall-climbing robots cannot directly use traditional energy consumption models due to the specificity of their structures.

ICM International Climbing Machines of the crawler type can move the planar geometry at high speeds. The ICM type is securely adhered as it impacts the machine over surface obstacles such as bolt heads, plates, weld seams, and other surface irregularities. The ICM type has an advantage to air leakage when dust, dirt, or uneven surfaces are in the air channel. The air channel on which the robot works is complex, characterized by unstructured environments with many pipe diameter changes, ramps, turnouts, bends, vertical obstacles such as support columns, and horizontal obstacles such as angle fixtures. It is difficult for the ICM type to turn flexibly to move around on the air channel, and the crawlers are prone to wear and tear due to the high friction between the tracks and the duct wall. The ICM type is prone to adhesion failure when crossing irregular obstacles.

After reading the literature, we found that wall-climbing robots with adhesion and obstacle-crossing capabilities have complex structures and consume large amounts of energy. To solve these problems, we will attempt to design a better robot structure with chain feet as the movement units to perform negative pressure adhesion. The Chain feet are superior in energy consumption due to their high vacuum pressure and low flow rate compared with ICM's low vacuum and high flow rate. The robot can drag 15 m of air hose to connect the external vacuum source. The robot can traverse 5 cm of unevenness between the surfaces. Compared with other robot structures, this robot has the ability of adhesion and obstacle-crossing through the alternating motion of the chain feet. Regarding the power consumption of the robot, the effects of relevant parameters such as the motor angular velocity, the friction coefficient, the sprocket pitch radius of the chain drive engagement, and the sprocket pitch radius of the chain drive engagement are investigated through kinetic analysis. The power model of the robot is established by combining the energy model of the drive motor and the power model of the transmission system.

The rest of this paper is divided into five sections. In Sect. 2, the structural design and the motion mechanism of the robot based on the chain feet with negative pressure adhesion are described. In Sect. 3, the mechanics model and the analysis of the mechanical simulation are presented. In Sect. 4, the energy model of the driving motor, the power model of the transmission system and the robot power model are provided. In Sect. 5, the influences of relevant design parameters on the power consumption of the robot are revealed and verified through simulation and experiment. Finally, in Sect. 6, the conclusions and future work are provided.

2 Robot model

2.1 Robot mechanism design

The structure of the wall-climbing robot consists of a motion module and an adhesion module, as shown in Figure 1. The motion module serves to ensure the free movement of the robot on the air channels in the hospital and can overcome obstacles. The adhesion module ensures the effective adhesion of the robot when it moves on the wall of an air channel. In the structure of the robot, the sprocket and ten adhesion feet that are evenly distributed

Fig. 1 Structure of the wall-climbing robot

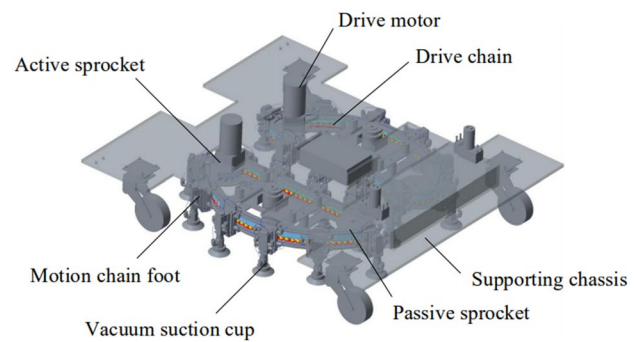
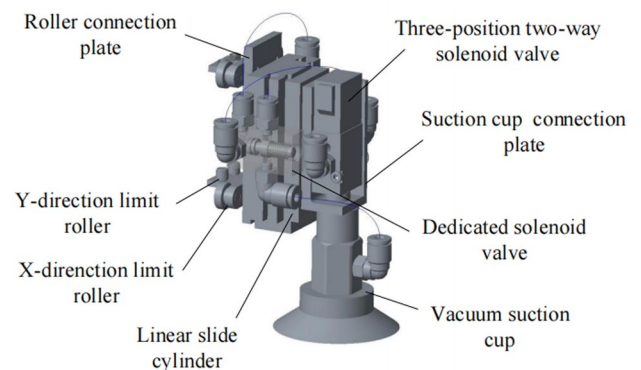


Fig. 2 Structure of a chain foot with negative pressure adhesion



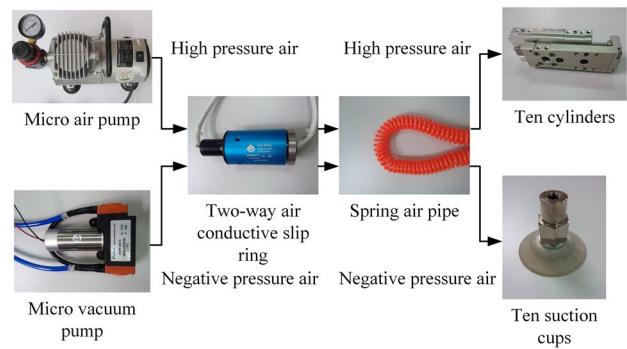
on the chain in the same plane form the mechanism of the chain feet, which makes the robot have the ability of motion adaptation.

The motion module includes a supporting chassis, a drive device, and motion chain feet. The drive device includes drive chains, active sprockets, passive sprockets, and drive motors connected to drive the rotation of the active sprocket. The drive chain is mounted on an active sprocket and a passive sprocket. The motion track of the drive chain includes a straight section and an arc section. The two ends of the straight section and the two ends of the arc section continuously and smoothly transition to form a closed curve. The motion chain feet are equally spaced and installed on the drive chain.

Figure 2 shows that the vacuum suction cup of the adhesion module is mounted on the lower end of the suction cup connection plate [17]. The suction cup connection plate is connected to the action end of the linear slide cylinder, which is used to drive the up and down action of the suction cup connection plate. The linear slide cylinder is mounted on the roller connection plate. Two X-direction limit rollers that match the X-direction limit guide on the frame and two Y-direction limit rollers that match the Y-direction limit guide on the frame are mounted on the top and bottom of the roller connection plate. The rotation directions of the X-direction limit roller and the Y-direction limit roller are perpendicular to each other. The air inlet of the suction cup is connected to an external device with negative pressure adhesion.

As shown in Fig. 3, the robot's air system is divided into two air paths: the high pressure air path and the negative pressure air path. A micro air pump generates high pressure air for the high pressure air path. To transmit the air path, it is necessary to use a conductive slip ring that can be vented with a retractable spring air pipe because the cylinders are fixed to the rotating movement of the chain foot. To meet the cylinders' operational requirements, the high pressure air will be transferred to the cylinders. A micro vacuum pump generates negative pressure air for the negative pressure air path. The negative pressure air is transferred to the suction cups on the chain foot by the conductive slip ring and spring air pipe in order to satisfy the suction cups' negative pressure requirements. The motion adhesion module of the robot is able to perform the functions of motion, adhesion, and barrier crossing due to the cooperation and synergistic action between the two air paths.

Fig. 3 The robot's air system



2.2 Analysis of the motion mechanism

The robot's electrical control system is shown in Fig. 4. The robot walking drive system consists of the motion chain feet and the motion chassis, which cooperate with each other to achieve robot walking motion. The motion chain foot uses the intermittent action of the suction cups and cylinders to complete the function of adsorbing and disengaging the surface of the air channels. The motion chain foot can enter the working state by using the system command to operate the solenoid valve of the cylinder. The solenoid valve of the cylinder can be opened, and the cylinder passes the high-pressure gas through the air pipe. Moreover, the cylinder slides down a certain stroke, and the suction cup is driven by the cylinder to move downward, making the suction cup and the wind pipe surface contact. The system command can then be used to open the solenoid valve of the suction cup. The air inside the suction cup is exhausted through the air pipe. Additionally, a certain negative pressure is generated inside and outside of the suction cup so that the motion chain foot of the robot adsorbs on the surface of the air channels. The adhesion state of the motion chain foot is shown in Fig. 5a.

When the motion chain foot needs to leave the wall, the system command controls the solenoid valve of the suction cup to shut off. The negative pressure inside the suction cup disappears, and the suction cup loses the adhesion force of the air channels. The system command controls the solenoid valve of the cylinder to power off. The solenoid valve of the cylinder changes the working position. The direction of the gas pressure changes in the cylinder. The cylinder is reset to the original state, which in turn causes the robot's feet to detach from the wall due to the negative pressure adhesion. The motion chain foot adhesion state is shown in Fig. 5b.

The motion chassis of the robot consists of two completely symmetrical chassis, each of which has an independent set of chain drive mechanisms, including motors, chains, and sprockets, as shown in Fig. 6. Ten chain feet are fixed on each chassis through the chain drive. The splicing of the two chassis forms the motion chassis of the robot. According to the different

Fig. 4 The robot's electrical control system

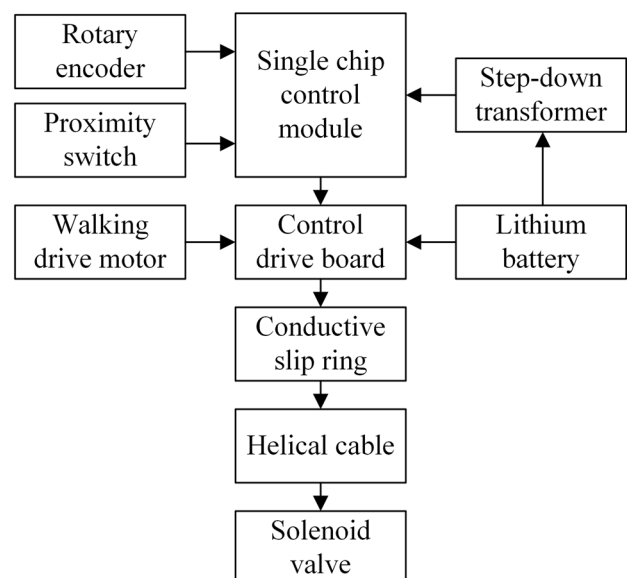
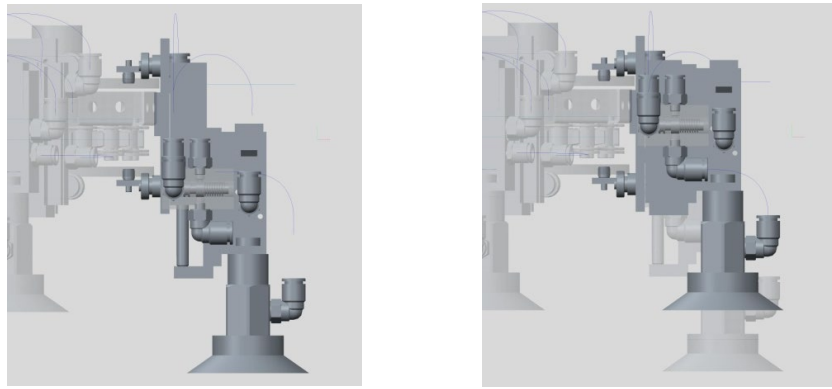


Fig. 5 Working principle of the motion chain foot



(a) Adhesion state of the motion chain foot (b) Disengagement state of the motion chain foot

instructions of the control system, the chain feet on the motion chassis can accomplish two forms of motion: linear walking and in situ rotation. According to these two forms of motion, we divided the twenty motion chain feet into two groups, namely, the walking foot group and the rotating foot group.

When the robot is prompted to perform straight-line walking, the walking feet are adsorbed on the air channels. The rotating feet are in the state of leaving the air channel. The chain drives the movement of the chain feet. The walking mechanism moves forward when the limit rollers of the adhesion feet slide on the chain frame because the chain feet are equipped with limit rollers. The layout of the chain feet when the robot walks in a straight line is shown in Fig. 7. When the robot needs to rotate in place, the rotating feet are adsorbed on the air channels and the walking feet are in the state of leaving the air channels.

In the actual environment, there are not only ideal surfaces, but also dust, dirt, and unevenness due to deterioration, which may make vacuum adhesion difficult. Due to the leakage of air between the suction cup and the wall, the flow rate of the functioning parts is lower than the flow rate of the pump's output. The total amount of leakage in the air pressure system is known as the system's volumetric loss. This is because a certain pressure difference causes the leakage, resulting in the loss of air pressure energy.

In the air pressure system, the air pressure loss and volumetric losses correspond to the air pressure efficiency η_{pne} and volumetric efficiency η_{vol} .

$$\eta_{pne} = \frac{P_{in} - \Delta p \cdot Q}{P_{in}} \quad (1)$$

Fig. 6 Motion chassis of the robot

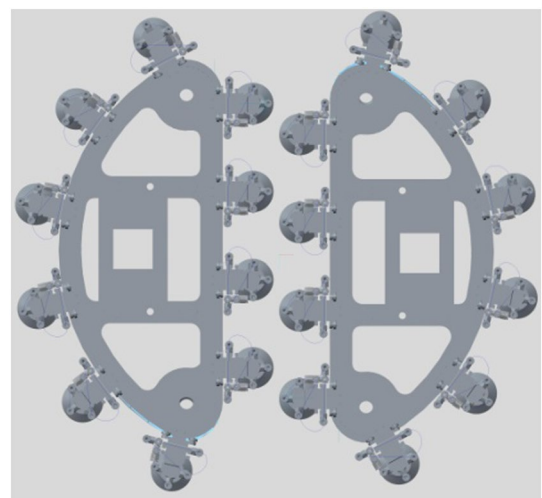
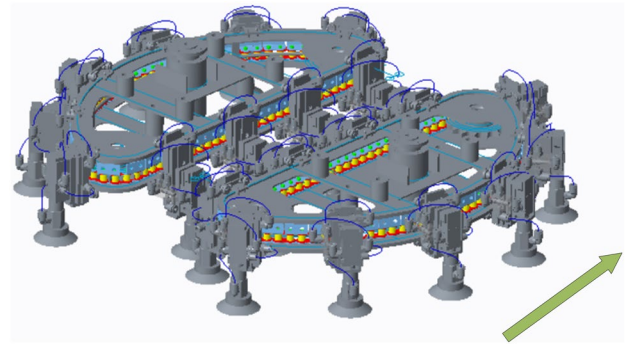


Fig. 7 Chain foot layout of a robot walking in a straight line



where $\Delta p \cdot Q$ represents the power loss by air pressure.

$$\eta_{vol} = \frac{P_{in} - q \cdot p}{P_{in}} \tag{2}$$

where q represents the leakage amount, $q \cdot p$ represents the power loss caused by leakage.

Figure 8 shows the force sketch of the negative pressure adhesion module of the robot. According to the force equilibrium relationship, the force equation of the negative pressure adhesion module is as follows.

$$\begin{cases} F_{Np} - G \cos \varphi - \sum_{i=1}^8 F_{pi} = 0 \\ G \sin \varphi - F_{fp} = 0 \\ F_{fp} = F_{Np} \mu_p \\ G = Mg \end{cases} \tag{3}$$

where F_{Np} represents the robot's support force, G represents the robot's gravity force, F_{pi} represents the adhesion caused by the pressure difference between the inside and outside of the suction cups to generate the force on the robot, φ represents the tilt angle of the wall and the ground, F_{fp} represents the robot's equivalent force subjected to the friction force, μ_p represents the coefficient of friction, M represents the weight of the robot.

The robot negative pressure adhesion force can be expressed as:

$$F_{p1} = \frac{Mg}{\mu_p} (\sin \varphi - \mu_p \cos \varphi) \tag{4}$$

The operating pressure requirement of the adhesion system for each suction cup of the robot is at least as:

Fig. 8 The force sketch of the negative pressure adhesion module of the robot

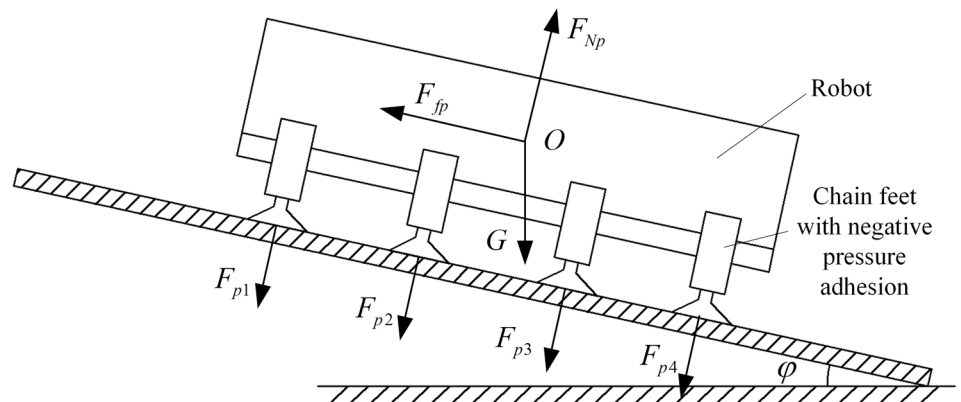


Fig. 9 Walking drive system of the robot

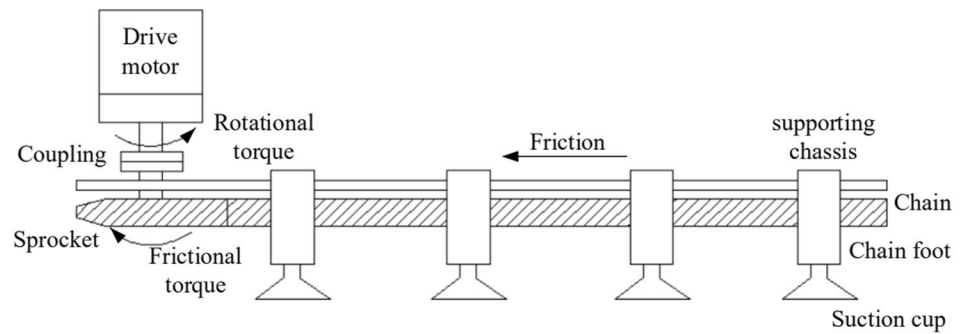
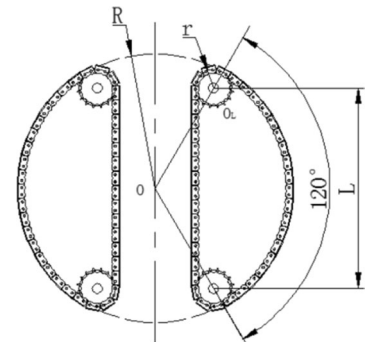


Fig. 10 Geometric model of the robot motion chassis



$$\Delta p = \frac{F_{p1}}{S_p} \tag{5}$$

where S_p represents the effective adhesion area of the suction cup.

3 Dynamics analysis of the robot

3.1 Mechanics model

The walking drive system of the robot converts the rotary motion of the drive motor into linear and rotary motion of the chain feet with negative pressure adhesion, as shown in Fig. 9. The drive motor is connected to the drive sprocket by a coupling. The chain feet with negative pressure adhesion rely on the chain to obtain the motion capability.

The chain drive of the motion chassis uses a combination of linear and circular segments, which enables the robot to move linearly or rotate in the motion chassis system of the walking drive system. The general method cannot be used to analyze the circumferential force of the chain drive because of the special structure. Therefore, an in-depth mechanical analysis of the drive mechanism is needed. The effective circumferential force F_A of the chain drive is related to the mechanism shape and the force situation of the motion chassis. The dynamics model of the motion chassis needs to be analyzed. The geometric model of the robot motion chassis should be established before creating the dynamics model of the robot motion chassis [18, 19]. The geometric model can be simplified because the chain feet are evenly arranged on the chain, as shown in Fig. 10. The forces on the motion chassis of the robot walking system are shown in Fig. 11. The basic physical parameters are shown in Table 1.

According to the equilibrium conditions of the system of particles, the mechanical equilibrium equation is obtained by combining the Alembert Principle and the Newton–Euler equation [20].

$$\begin{cases} \sum F_i^e + \sum F_{gi} = 0 \\ \sum m_j(F_j^e) + \sum m_j(F_{gi}) = 0 \end{cases} \tag{6}$$

Fig. 11 Power analysis of the robot motion chassis

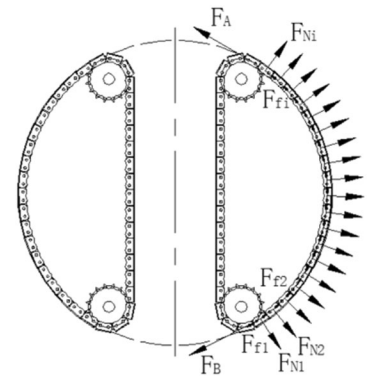


Table 1 Basic physical parameters

| Symbols | Physical parameters |
|----------|--|
| O | Walking System Origin |
| O_L | Active Sprocket Center of the Drive Chain |
| L | Center Distance of the Chain Drive |
| R | Robot Rotation Radius |
| r | Pitch Circle Radius of the Sprocket |
| F_A | Effective Circumferential Force of the Chain Drive |
| F_B | Passive Sprocket Resistance |
| F_{Ni} | Support Force of i Chain Link on the Baffle |
| F_{fi} | Frictional Resistance of i Link |

where F_i^e represents the external force on Particle i , F_{gi} represents the inertia force of Particle i , $m_j(F_i^e)$ represents the external moment of Particle i with respect to the j -axis and $m_j(F_{gi})$ represents the moment of inertia of Particle i with respect to the j -axis.

The analysis of the forces on the robot motion chassis is the basis for establishing the power model of the mechanical transmission system. The force situation of the robot motion chassis includes i support forces F_{Ni} and i friction forces F_{fi} , as shown in Fig. 11. However, the combined force value cannot be obtained with different force values. Moreover, the overall force balance analysis of the robot motion chassis cannot be performed. Thus, the force analysis of the chain drive link is needed. The force balance analysis of the chain drive links is shown in Fig. 12.

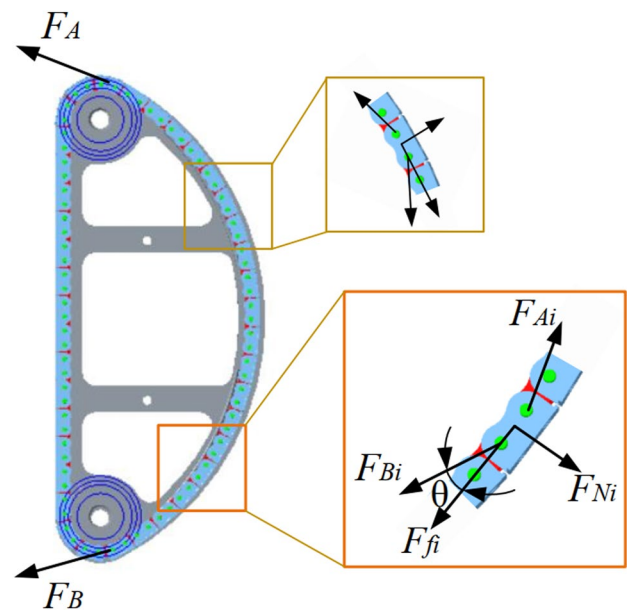
A single chain link of the robot motion chassis is used as the object of study. The coordinate system is established with the center point as the origin for the force analysis of the chain link. The mechanical equations of the single chain link of the robot motion chassis are established as follows.

$$\begin{cases} F_{Ai} \sin\theta + F_{Bi} \sin\theta - F_{Ni} = \Delta m \omega_R^2 R \\ F_{Ai} \cos\theta = F_{Bi} \cos\theta + \mu_N F_{Ni} \\ F_{Bi} = F_{A(i-1)} \\ \omega_R = \frac{r}{R} \omega_{ch} = \frac{r}{K_g R} \omega_d \end{cases} \quad (7)$$

Equation (2) of the force balance can be simplified since the forces are mutual. The mechanical equation for a single link can be obtained as follows:

$$\begin{cases} F_{Ai} = k_1 F_{A(i-1)} - k_2 \omega_d^2 \\ k_1 = \frac{(\cos\theta + \mu_N \sin\theta)}{(\cos\theta - \mu_N \sin\theta)} \\ k_2 = \frac{\mu_N \Delta m r^2}{K_g^2 R (\cos\theta - \mu_N \sin\theta)} \end{cases} \quad (8)$$

Fig. 12 Force balance analysis of a chain drive link



The effective circumferential force of the chain drive is introduced through the analysis of the equilibrium equation of the force system.

$$F_A = k_1^{n-1} F_B - k_2 \omega_d^2 \sum_{i=2}^n k_1^{i-2} \tag{9}$$

3.2 Analysis of the mechanical simulation

The circumferential force of the chain drive is simulated to analyze the effect of each design parameter of the robot on the force characteristics of the drive. The circumferential force of the chain drive increases with the increase in the friction coefficient of the mechanism and is less influenced by the angular velocity of the drive motor, as shown in Fig. 13. The radius r of the pitch circle of the chain drive engagement and the rotation radius R of the robot drive system are important parameters for the design of the robot mechanism. Their effects on the magnitude of the circumferential force of the chain drive need to be analyzed. The circumferential force of the chain drive is less influenced by the radius r of the pitch circle and the rotation radius R of the robot drive, as shown in Fig. 14.

Fig. 13 Relationships between the circumferential force and friction coefficient and motor angular velocity

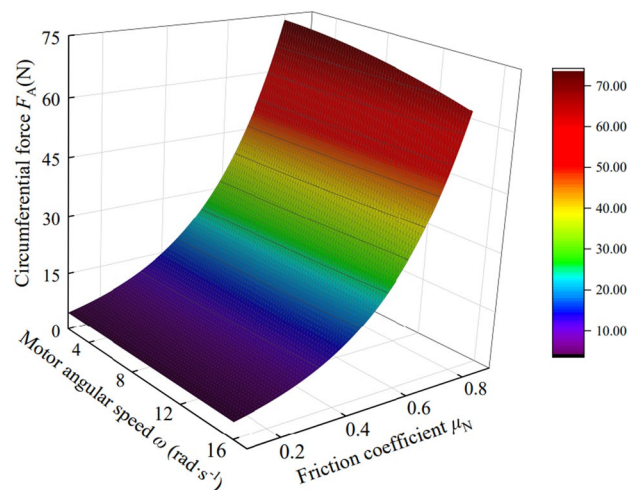
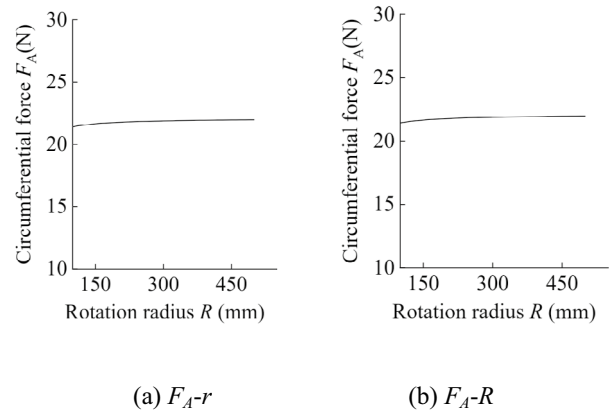


Fig. 14 Simulation of the circumferential force of the chain drive



4 Power model of the robot

4.1 Energy model of driving motor

To analyze the robot’s power characteristics, the energy model of the drive motor and the power model of the drive system need to be combined. The drive motor is the main power source for robot motion. When the robot is operating in steady state, the mechanical characteristics of the drive motor [21] can be expressed as:

$$\begin{cases} n = \frac{U_a}{C_e \Phi} - \frac{R_a}{C_e \Phi} I_a \\ M_e = C_M \Phi I_a \\ P_i = R_a I_a^2 + E_a I_a = U_a I_a \end{cases} \quad (10)$$

where U_a represents the armature voltage, I_a denotes the armature current, R_a represents the armature resistance, C_e represents the electromotive force coefficient, C_M represents the electromagnetic torque coefficient, Φ represents the main magnetic flux, M_e represents the electromagnetic torque, and P_i represents the motor input power.

The drive motor has good speed regulation performance. Its input power, velocity, and electromagnetic torque are all related to the armature current. The model equation of the energy transfer of the drive motor can be obtained as

$$\begin{cases} M_e(I_a)\omega = \alpha_i P_c + M_0 \omega + B\omega^2 + J\omega \frac{d\omega}{dt} \\ \omega = \frac{\pi}{30} n = \omega(I_a) \\ P_i = P_i(I_a) \end{cases} \quad (11)$$

where ω represents the angular velocity.

A direct relationship can also be established between the armature current and the angular velocity with a certain voltage at the armature end of the drive motor.

$$I_a = -\frac{C_e \Phi}{R_a} n + \frac{U_a}{R_a} = -\frac{C_e \Phi}{R_a} \cdot \frac{30}{\pi} \omega + \frac{U_a}{R_a} \quad (12)$$

The energy transfer model of the robot drive motor can be obtained by combining Eq. (6) and Eq. (7).

$$\begin{cases} M_e[I_a(\omega)]\omega = M_e'[\omega]\omega \\ = \alpha_i P_c + M_0 \omega + B\omega^2 + J\omega \frac{d\omega}{dt} \\ I_a = I_a(\omega) \\ P_i = P_i[I_a(\omega)] = P_i'(\omega) \end{cases} \quad (13)$$

4.2 Power model of the transmission system

The power model of the transmission system is established based on the analysis of the kinetic model [22]. The load torque T_t of the chain drive can be obtained by establishing the mechanical analysis of the motor shaft, drive coupling, and chain drive.

$$\begin{cases} T_d = J_d \frac{d\omega_d}{dt} + B_d \omega_d + T_l \\ T_l = J_a \frac{d\omega_d}{dt} + \frac{1}{K_g} T_{ch} \\ T_{ch} = J_{ch} \frac{d\omega_{ch}}{dt} + T_t \\ T_t = r F_t \end{cases} \quad (14)$$

where J_d represents the rotational inertia of the driving motor, ω_d represents the shaft velocity of the drive motor, B_d represents the damping factor of the driving motor, T_l represents the coupling torque, J_a represents the coupling inertia, K_g represents the coupling transmission ratio, T_{ch} represents the chain drive torque, J_{ch} represents the sprocket inertia, ω_{ch} represents the sprocket velocity and F_t represents the force of the chain drive system.

The mechanical equations are established by analyzing the system force F_t of the chain drive, centrifugal tension F_c of the chain drive and friction resistance F_f of the chain drive [23].

$$\begin{cases} F_t = (M_t + M_{load}) \frac{dv_{ch}}{dt} + F_A + F_c + F_f + F_{ext} \\ F_c = \frac{r^2 q}{K_g^2} \omega_d^2 \\ F_f = (M_t + M_{load}) g \mu_m \end{cases} \quad (15)$$

where M_t represents the robot body weight, M_{load} represents the robot load weight, and F_{ext} represents the additional resistance of transmission.

The force on the chain drive system can be obtained after the above detailed analysis of the forces on the chain drive.

$$\begin{cases} F_t = (M_t + M_{load}) \frac{dv_{ch}}{dt} + F_A + F_c + F_f + F_{ext} \\ = \frac{r}{K_g} (M_t + M_{load}) \frac{dv_d}{dt} + k_1^{n-1} F_B - k_2 \omega_d^2 \sum_{i=2}^n k_1^{i-2} \\ \quad + \frac{r^2 q}{K_g^2} \omega_d^2 + (M_t + M_{load}) g \mu_m + F_{ext} \end{cases} \quad (16)$$

where μ_m represents the friction coefficient in the robot drive process.

The output torque equation of the drive motor can be obtained after substituting the chain drive force F_t into the load torque Eq. (9) of the chain drive.

$$\begin{cases} T_d = J_d \frac{d\omega_d}{dt} + B_d \omega_d + T_l \\ = [J_d + J_a + \frac{1}{K_g^2} J_{ch} + \frac{r^2}{K_g^2} (M_t + M_{load})] \frac{d\omega_d}{dt} \\ \quad + \frac{r}{K_g} \left(\frac{r^2 q}{K_g^2} - k_2 \sum_{i=2}^n k_1^{i-2} \right) \omega_d^2 + B_d \omega_d \\ \quad + \frac{r}{K_g} [k_1^{n-1} F_B + (M_t + M_{load}) g \mu_m + F_{ext}] \end{cases} \quad (17)$$

The input power of the robot travel system can be obtained as follows when the travel speed is stable.

$$\left\{ \begin{aligned} P_{out} = T_d \omega_d &= \frac{r}{K_g} \left(\frac{r^2 q}{K_g^2} - k_2 \sum_{i=2}^n k_1^{i-2} \right) \omega_d^3 + B_d \omega_d^2 \\ &+ \frac{r}{K_g} [k_1^{n-1} F_B + (M_t + M_{load}) g \mu_m + F_{ext}] \omega_d \\ k_1 &= \frac{(\cos\theta + \mu_N \sin\theta)}{(\cos\theta - \mu_N \sin\theta)} \\ k_2 &= \frac{\mu_N \Delta m r^2}{K_g^2 R (\cos\theta - \mu_N \sin\theta)} \end{aligned} \right. \quad (18)$$

4.3 Robot power model

The power of the robot system includes the drive power and various losses according to the energy consumption characteristics of the robot. The robot power can be expressed as the sum of the motor drive power P_d and the system loss P_{Le} .

$$\left\{ \begin{aligned} P_1 &= P_d + P_{Le} \\ P_d &= T_e \omega_d \\ T_e &= K_T I_a \\ T_e &= T_d + T_0 \end{aligned} \right. \quad (19)$$

The loss of electric power in the drive motor, which consists of various losses in the motor, can be simplified as:

$$\left\{ \begin{aligned} P_{Le} &= P_0 + 2p \Delta U_b I_a + b \left(\frac{I_a}{I_N} \right)^2 \\ b &= P_N \left(\frac{1}{\eta_c} - 1 \right) - 2p \Delta U_b I_N - P_0 \end{aligned} \right. \quad (20)$$

where b represents the coefficient of electric loss, P_0 represents the motor no-load power, p represents the number of motor pole pairs, ΔU_b represents the drop in contact voltage and η_c represents the motor rated efficiency.

The motor armature current equation can be obtained by substituting the torque equation.

$$\begin{aligned} I_a = \frac{1}{K_T} T_e &= \frac{1}{K_T} \left\{ \frac{r}{K_g} \left(\frac{r^2 q}{K_g^2} - k_2 \sum_{i=2}^n k_1^{i-2} \right) \omega_d^2 + B_d \omega_d \right. \\ &\left. + \frac{r}{K_g} [k_1^{n-1} F_B + (M_t + M_{load}) g \mu_m + F_{ext}] + T_0 \right\} \end{aligned} \quad (21)$$

The robot power model equation can be obtained by combining Eqs. (13) to (15).

$$P_1 = P_d + P_{Le} = K_3 \omega_d^4 + K_4 \omega_d^3 + K_5 \omega_d^2 + K_6 \omega_d + K_7 \quad (22)$$

The simulation analysis of the robot power model shows that the total system power P_1 increases with an increasing angular velocity ω_d and load mass M , as shown in Fig. 15.

5 Results and discussion

The robot prototype is shown in Fig. 16. The mass of the robot body is 10.5 kg, and the dimensions are L650 mm, W530 mm, and H260 mm. Regarding one chain foot with negative pressure adhesion, the mass is 0.09 kg, the quantity is 20, and the dimensions are L85 mm, W72 mm, and H110 mm. The dimension of the vacuum suction cup is 55 mm. The power of the motor is 25 W, and the rotational speed is 1800 r/min. PWM voltage regulation is used for robot velocity regulation in the experiment to verify the accuracy of the robot power model. The oscilloscope is used to monitor the output values of the drive motor governor in real time to prevent the velocity regulation signal from being disturbed or changed during the experiment [24]. The angular velocity of the drive motor is obtained by collecting data from the rotary encoder [18].

The robot's motion is shown in Fig. 17. When the robot is prompted to perform straight-line walking, the walking feet are adsorbed on the air channels. The rotating feet are in the state of leaving the air channels. When the robot needs to rotate in place, the rotating feet are adsorbed on the air channels and the walking feet are in the state of leaving the air channels. Figure 15 shows that the angular velocity of the drive motor and the load mass of the robot have a large

Fig. 15 Relationships between the robot power and motor angular velocity and load mass

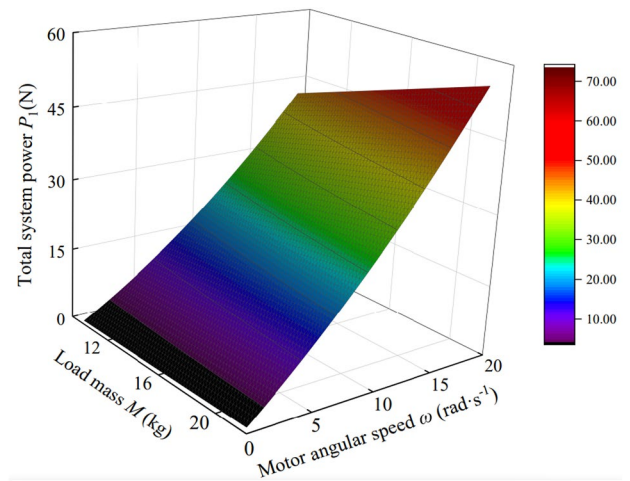


Fig. 16 Robot prototype

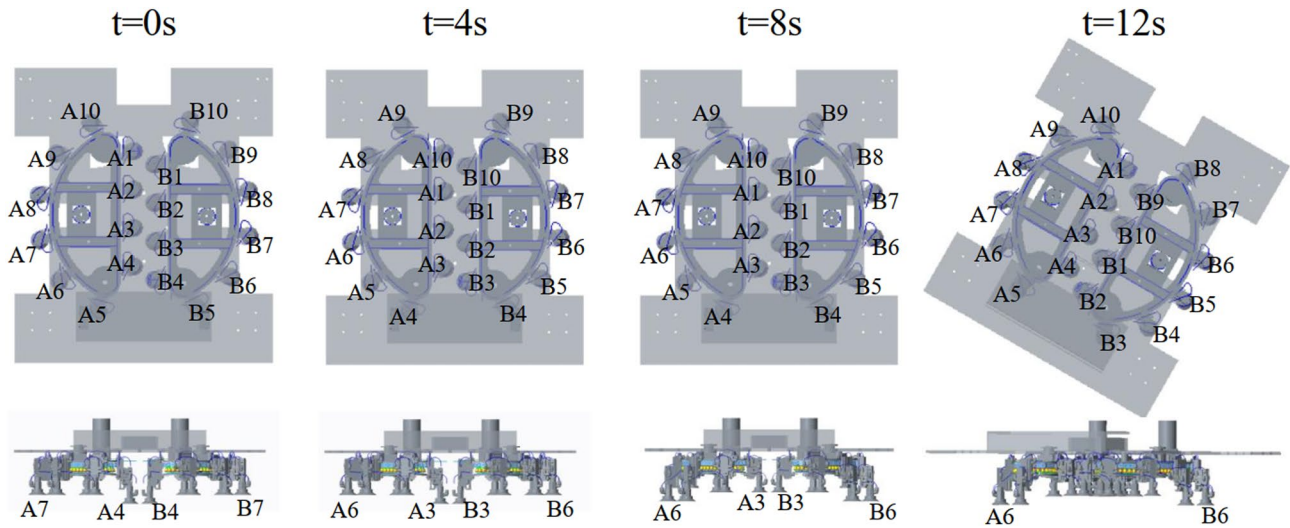
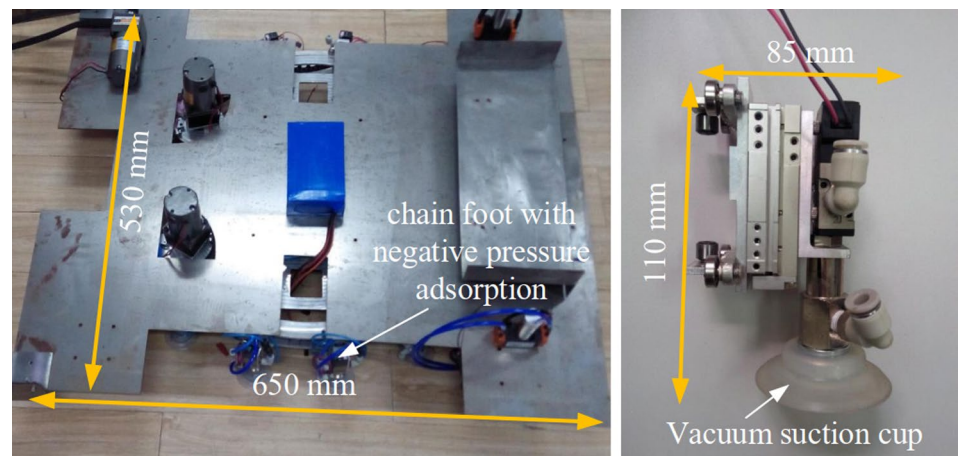


Fig. 17 Robot's motion

influence on the power consumption of the robot from the simulation results. The experiments are conducted under no-load and loaded conditions to analyze the effects of the angular velocity of the drive motor and the load mass of the robot on the power consumption of the robot. Moreover, we determined that the measured motor current is larger than

the simulated values by comparing the simulated armature current with the measured motor current. Motor losses are reflected by an increase in the current.

The trends of the no-load power and the on-load power of the robot system are basically consistent with the simulation results, as shown in Fig. 18. The measured average power with load is 28.1 W, which is close to the simulation result of 27.3 W. The fluctuation of the actual measured values is mainly due to the uneven distribution of the running resistance of the robot motion chassis during the experiment. The intermittent running hindrance causes the output current to fluctuate. The robotic designs must be lightweight. The mechanism and hardware that are made of lightweight materials can reduce the power consumption of the robot and achieve the optimization of the robot energy.

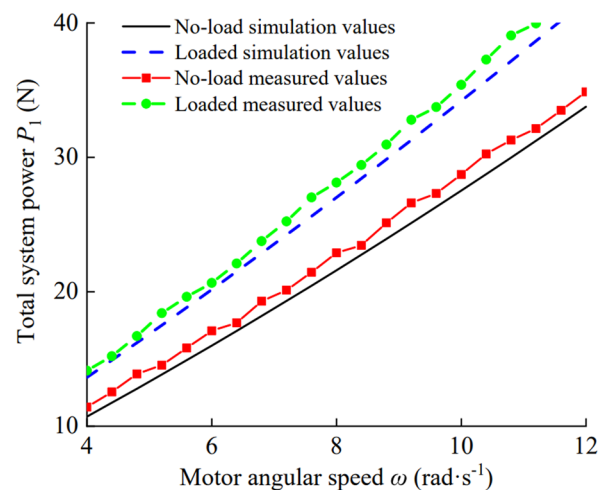
The aim of this research is to design a new wall-climbing robot. The findings show that this wall-climbing robot has a unique motion module using chain feet with negative pressure adhesion as the motion units. The twenty motion chain feet are divided into two groups: the walking foot group and the rotating foot group. It is also revealed that the individual design parameters of the motion module of this robot have different effects on its mechanical properties. The circumferential force of the chain drive increases with the increase in the friction coefficient of the mechanism and is less influenced by the angular velocity of the drive motor. The circumferential force of the chain drive is less influenced by the radius r of the pitch circle and the rotation radius R of the robot drive. The proposed robot power model is also a distinctive feature of this study.

The structure of the wall climbing robot in this paper is smaller in size and more compact compared to those proposed by other scholars [9, 25]. The structure of the wall-climbing robot designed in this paper has special characteristics. Different combinations of chain feet with negative pressure adhesion can correspond to different motion states. The robot power model proposed by other scholars focuses on robot operation and path planning [14, 26]. The power model in this paper further reveals the relationship between the robot power and design parameters. It also complements the factors influencing the robot power model. These results are very significant in advancing the in-depth study of robot design optimization and control optimization.

6 Conclusions

- (1) A robot power model is established based on the dynamics analysis method by combining the energy model of the drive motor and the power model of the transmission system to provide a theoretical basis for the optimal design of the robot.
- (2) The robot motion mechanism is analyzed. The effects of relevant parameters, such as the motor angular velocity, friction coefficient, sprocket pitch radius of the chain drive engagement, and sprocket pitch radius of the chain drive engagement, on the mechanical characteristics of the robot are revealed.
- (3) Simulations and experiments are used to study the effects of the parameters such as the robot load and motor angular velocity on the robot power consumption. The results show that the robot power model is consistent with the actual situation. The power consumption of the robot can be reduced by adjusting the parameters.

Fig. 18 Curve of the robot power



The robot power model can be used to guide the optimal design of robot performance. Parameters involved in the model, such as the motor angular velocity, help establish the corresponding control model and energy optimization. Notably, the limitation of this study is that the analysis of the energy model of the robot in this paper mainly focuses on the robot motion module and has not been combined with functional modules such as cleaning, which requires further improvement of the robot structure and its energy model. On the other hand, the robot in this paper lacks motion control and has no path planning to verify the energy optimization under different motions. In future work, we will further study the automatic cleaning and disinfection of air channels in hospitals with the detection probe, the cleaning module and the disinfection module to achieve comprehensive coverage.

Author contributions All authors contributed to the study conception and design. Material preparation, data collection and analysis were performed by Zhen Qian. The first draft of the manuscript was written by Hanbiao Xia and all authors commented on previous versions of the manuscript. All authors read and approved the final manuscript.

Funding This work was supported by the Fundamental Research Project for the Wenzhou Science & Technology Bureau under Y20220803.

Data availability All data analyzed during this study are included in this published article.

Declarations

Competing interests The authors declare that there is no conflict of interest regarding the publication of this paper.

Open Access This article is licensed under a Creative Commons Attribution 4.0 International License, which permits use, sharing, adaptation, distribution and reproduction in any medium or format, as long as you give appropriate credit to the original author(s) and the source, provide a link to the Creative Commons licence, and indicate if changes were made. The images or other third party material in this article are included in the article's Creative Commons licence, unless indicated otherwise in a credit line to the material. If material is not included in the article's Creative Commons licence and your intended use is not permitted by statutory regulation or exceeds the permitted use, you will need to obtain permission directly from the copyright holder. To view a copy of this licence, visit <http://creativecommons.org/licenses/by/4.0/>.

References

1. Xu S, He B, Hu H. Research on kinematics and stability of a bionic wall-climbing hexapod robot. *Appl Bionics Biomech*. 2019. <https://doi.org/10.1155/2019/6146214>.
2. Silva MF, Barbosa RS, Oliveira ALC. Climbing robot for ferromagnetic surfaces with dynamic adjustment of the adhesion system. *J Robotics*. 2012. <https://doi.org/10.1155/2012/906545>.
3. Alkalla MG, Fanni MA, Mohamed AF, Hashimoto S, Hamed A. EJBot-II: an optimized skid-steering propeller-type climbing robot with transition mechanism. *Adv Robot*. 2019;4:1–18. <https://doi.org/10.1080/01691864.2019.1657948>.
4. Howlader MDOF, Sattar TP. Finite element analysis based optimization of magnetic adhesion module for concrete wall climbing robot. *Int J Adv Comput Sci Appl*. 2015;6(8):8–18. <https://doi.org/10.14569/ijacsa.2015.060802>.
5. Chattopadhyay P, Ghoshal SK. Adhesion technologies of bio-inspired climbing robots: a survey. *Int J Robot Autom*. 2018;33(6):654–61. <https://doi.org/10.2316/Journal.206.2018.6.206-5193>.
6. Xue C, Wang H, Chen Y. Optimal design and experiment of a wall-climbing robot with thrust adsorption. *J Zhejiang Univ (Eng Sci)*. 2022;56(06):1181–90.
7. Murphy MP, Tso W, Tanzini M, Sitti M. Waalbot: An agile small-scale wall climbing robot utilizing pressure sensitive adhesives. *IEEE/RSJ Int Conf Intell Robots Syst*. 2006;2006:3411–6. <https://doi.org/10.1109/IROS.2006.282578>.
8. Saberland V, Ghorbanirezaei S, Hoggat Y. Testing the application of Free Flapping Foils (FFF) as a method to improve adhesion in an electrostatic wall-climbing robot. *J Adhes Sci Technol*. 2019;33(23):2579–94. <https://doi.org/10.1080/01694243.2019.1653026>.
9. Dong H, Cui DQ, Li FX, Gao XS. Design and analysis of multi-suction cup frame wall-climbing robot system. *Manuf Autom*. 2016;38(6):59–63.
10. Gao Y, Wei W, Wang X, Li Y, Wang D, Yu Q. Feasibility, planning and control of ground-wall transition for a suctorial hexapod robot. *Appl Intell*. 2021;51:5506–24. <https://doi.org/10.1007/s10489-020-01955-2>.
11. Tovarnov MS, Bykov NV. A mathematical model of the locomotion mechanism of a mobile track robot with the magnetic-tape principle of wall climbing. *J Mach Manuf Reliab*. 2019;48:250–8. <https://doi.org/10.3103/S1052618819030130>.
12. Nemoto T, Mohan RE, Iwase M. Rolling locomotion control of a biologically inspired quadruped robot based on energy compensation. *J Robotics*. 2015. <https://doi.org/10.1155/2015/649819>.
13. Chen D, Zhang J, Weng X, Zhan Y, Shi Z. Analysis of stiffness and energy consumption of nonlinear elastic joint legged robot. *Appl Bionics Biomech*. 2020. <https://doi.org/10.1155/2020/8894399>.
14. Jaramillo-Morales MF, Dogru S, Gomez-Mendoza JB, Marques L. Energy estimation for differential drive mobile robots on straight and rotational trajectories. *Int J Adv Rob Syst*. 2020;17(2):1729881420909654. <https://doi.org/10.1177/1729881420909654>.
15. He Y, Mei J, Fang Z, Zhang F, Zhao Y. Minimum energy trajectory optimization for driving systems of palletizing robot joints. *Math Problems Eng*. 2018. <https://doi.org/10.1155/2018/7247093>.

16. MahmoudZadeh S, Powers DMW, Sammut K, Atyabi A, Yazdani A. A hierarchal planning framework for AUV mission management in a spatiotemporal varying ocean. *Comput Electr Eng*. 2018;67:741–60. <https://doi.org/10.1016/j.compeleceng.2017.12.035>.
17. Kim Y, Singh T. Energy-time optimal control of wheeled mobile robots. *J Franklin Inst*. 2022;359(11):5354–84. <https://doi.org/10.1016/j.jfranklin.2022.05.032>.
18. Fouad H, Beltrame G. Energy autonomy for robot systems with constrained resources. *IEEE Trans Rob*. 2022;38(6):3675–93. <https://doi.org/10.1109/TRO.2022.3175438>.
19. Kyaw PT, Le AV, Veerajagadheswar P, Elara MR, Thu TT, Nhan NHK, Vu MB. Energy-efficient path planning of reconfigurable robots in complex environments. *IEEE Trans Rob*. 2022;38(4):2481–94. <https://doi.org/10.1109/TRO.2022.3147408>.
20. Department of Theoretical Mechanics, Institute H, of Technology. *Theoretical Mechanics*. Beijing: Higher Education Press; 2020.
21. Liu F, Xu Z, Dan B. *Energy characteristics of machining systems and their applications*. Beijing: Machinery Industry Press; 1995.
22. Jeong YH, Min BK, Cho DW, Lee SJ. Motor current prediction of a machine tool feed drive using a component-based simulation model. *Int J Precis Eng Manuf*. 2010;11:597–606. <https://doi.org/10.1007/s12541-010-0069-1>.
23. Cheng D. *Mechanical Design Manual*, vol. 3. Beijing: Chemical Industry Press; 2017.
24. Muthugala MAVJ, Samarakoon SMBP, Elara MR. Toward energy-efficient online complete coverage path planning of a ship hull maintenance robot based on gladius bio-inspired neural network. *Expert Syst Appl*. 2022;187: 115940. <https://doi.org/10.1016/j.eswa.2021.115940>.
25. Liu Y, Lim B, Lee JW, Park J, Kim T, Seo T. Steerable dry-adhesive linkage-type wall-climbing robot. *Mech Mach Theory*. 2020;153: 103987. <https://doi.org/10.1016/j.mechmachtheory.2020.103987>.
26. Gürgöze G, TÜRKÖĞLU İ. A novel energy consumption model for autonomous mobile robot. *Turk J Electr Eng Comput Sci*. 2022;30(1):216–32. <https://doi.org/10.3906/elk-2103-15>.

Publisher's Note Springer Nature remains neutral with regard to jurisdictional claims in published maps and institutional affiliations.